Journal of
Materials Chemistry A

ROYAL SOCIETY OF CHEMISTRY

PAPER

View Article Online
View Journal | View Issue

Cite this: *J. Mater. Chem. A*, 2025, **13**, 41260

Integration of p-type-doped carbon nanostructures as additives for boosting spiro-OMeTAD performance in perovskite solar cells

Abbas Ahmad Khan, †[a] Helena Uceta, †[b] Javier Urieta-Mora, [ac] Manuel Pérez-Escribano, [d] Sara Abdollahzadeh,[a] Myriam Barrejón, [b] Joaquín Calbo, [d] Enrique Ortí, *[d] Fernando Langa *[b] and Nazario Martín *[ac]

Received 2nd September 2025
Accepted 23rd October 2025

DOI: 10.1039/d5ta07147j

rsc.li/materials-a

The application of chemically modified carbon nanotubes (CNTs) and nanohorns (CNHs) for perovskite solar cells (PSCs) has been almost limited to their use as electrodes, underutilizing their potential as charge-selective transporting materials. In this work, a comprehensive study of the implementation of carbon nanomaterials (CNMs) as additives for spiro-OMeTAD is presented. A detailed chemical characterization of the hybrid carbon nanostructures is performed, including optoelectronic and thermal properties, showing the potential of the modified CNMs to be implemented in photovoltaic devices. The incorporation of CNMs into spiro-OMeTAD induces an energy shift of the spiro-OMeTAD energy levels, optimizing the energy band alignment with the perovskite when spiro-OMeTAD is combined with porphyrin-functionalized single-wall CNTs (SWCNTs). CNM-doped spiro-OMeTAD resulted in improved power conversion efficiencies (PCEs) in comparison to the reference devices, reaching a maximum PCE of 19.8% for zinc-metalated porphyrin (ZnP)-SWCNT hybrids. The PCE enhancement is primarily attributed to the improved morphology and contact interface of the perovskite/hole-transporting material (HTM) layer, as well as to the increased hole mobility. Furthermore, stability tests show an improvement in the stability under ambient storage for the cells incorporating porphyrin-functionalized SWCNTs compared to the reference device, which is ascribed to the higher hydrophobicity resulting from the presence of CNMs.

Introduction

Since the ground breaking report of Miyasaka and co-workers in 2009,[1] perovskite solar cells (PSCs) have emerged as the most promising technology to complement silicon-based devices, reaching nowadays power conversion efficiencies (PCEs) of up to 27.0%.[2] Despite their outstanding photovoltaic performance, comparable to the best-performing silicon-based devices, the lack of long-term stability hinders the rapid implementation of PSCs in the photovoltaic market. In this context, the introduction of complementary materials and additives in the fabrication of the devices is envisioned as an important approach to enhance device stability.[3,4] Carbon nanomaterials (CNMs) have attracted the attention of the scientific community in the field of materials science for their potential application in optoelectronic devices. While fullerene derivatives have been successfully introduced in the field of photovoltaics due to their exceptional electron-accepting character, other nanostructures such as carbon nanotubes (CNTs), graphene or carbon nanohorns (CNHs) are still far from implementation in the photovoltaic field. The exceptional charge carrier properties of graphene and CNTs, along with their superior chemical and mechanical stability, make these alternative CNMs ideal materials for enhancing the long-term stability of photovoltaic devices, mainly in the case of PSCs.

The efficient integration of CNMs into PSCs has mostly been limited to the use of fullerene derivatives as efficient organic electron-transporting layers (ETLs) in inverted devices, the most prominent being derivatives such as $PC_{61}BM$, although some fullerene materials have also been incorporated as hole-transporting materials (HTMs) or additives.[5–11] Due to their excellent chemical and mechanical stability, the use of CNMs has typically focused on replacing standard transparent and/or metallic counter electrodes[12–16] and in semi-transparent PSCs.[17] Only a few examples employing functionalized single-walled CNTs

---

[a] IMDEA-Nanociencia, Faraday, 9, Campus de Cantoblanco, 28049 Madrid, Spain. E-mail: nazmar@quim.ucm.es

[b] Instituto de Nanociencia, Nanotecnología y Materiales Moleculares (INAMOL), Universidad de Castilla-La Mancha, Avenida Carlos III s/n, 45071 Toledo, Spain. E-mail: fernando.langa@uclm.es

[c] Departamento Química Orgánica, Facultad Ciencias Químicas, Universidad Complutense de Madrid, Av. Complutense s/n, 28040 Madrid, Spain. E-mail: nazmar@quim.ucm.es

[d] Instituto de Ciencia Molecular, Universidad de Valencia, Catedrático José Beltrán 2, 46980 Paterna, Spain. E-mail: enrique.orti@uv.es

† These authors contributed equally to this work.

(SWCNTs) or CNHs as charge transporting layers have been reported in recent years,[18–20] achieving moderate PCE values. In contrast, one of the most effective applications of CNMs has been their incorporation as additives or dopants, either within the active layer or in combination with charge-transporting layers. This approach leverages their p-type semiconducting nature, exceptional electrical conductivity, and high stability, resulting in significant enhancements in both device performance and operational stability.[21–24]

Despite the different architectures and configurations used to incorporate CNMs into PSCs,[23,25,26] the incorporation of functionalized CNMs has been scarcely explored. Existing studies have primarily focused on functionalizing CNMs with small molecular units, such as oxidized or amino derivatives.[16,21,27,28] These functional groups address dispersibility issues and improve interfacial adhesion with the hole transport material. However, they do not significantly alter the electronic structure of CNTs or markedly enhance the hole-transport properties of the hole-transporting layer (HTL). By contrast, the covalent attachment of electron-donating, highly conjugated systems such as triphenylamine or porphyrin derivatives is anticipated to promote more efficient and selective hole transport. This approach offers a promising strategy to optimize energy-level alignment for hole injection and to reduce interfacial recombination, in direct contrast to the limited effects offered by small molecular units.

Herein, we report the efficient incorporation of chemically modified CNMs, including donor *p*-methoxytriphenylamine-based (TPAOMe) CNHs and SWCNTs, and porphyrin-containing SWCNTs as additives for the reference compound 2,2′,7,7′-tetrakis(*N*,*N*-di(4-methoxyphenyl)amino)-9,9′-spirobifluorene, most well-known as spiro-OMeTAD. The newly reported CNMs have been prepared through [2 + 1] cycloaddition reactions involving nitrene intermediates, which are generated from the corresponding TPAOMe and *meso*-substituted-porphyrin azides, and the respective carbon nanostructures (SWCNTs or CNHs). [2 + 1] Cycloaddition reactions are the preferred method for the covalent modification of carbon CNMs due to their ability to anchor different derivatives without disrupting the intrinsic π-conjugated structure of the CNM surface. Unlike other covalent approaches such as [3 + 2] or [2 + 2] cycloadditions, a key advantage of the [2 + 1] cycloadditions is that it allows for the tuning of CNM properties without significantly deteriorating their exceptional electrical properties.[29] A comprehensive chemical characterization of the modified CNMs is presented, including thermogravimetric analysis (TGA), Raman spectroscopy, UV-vis absorption spectroscopy, photoluminescence (PL) spectroscopy, X-ray photoelectron spectroscopy (XPS), and density functional theory (DFT) calculations. Finally, the incorporation of the modified CNMs as spiro-OMeTAD additives into the PSC devices demonstrates an enhancement in both open-circuit voltage (V_{OC}) and fill factor (FF), with the SWCNTs functionalized with TPAOMe and Zn-porphyrin showing the highest performance. A maximum PCE of 19.8% was achieved, notably higher than that of the reference device employing non-doped spiro-OMeTAD, which exhibited a PCE of 18.0%. The notable improvement can be attributed to the better interface contact, enhanced morphology, and higher charge extraction, as evidenced by scanning electron microscopy (SEM) images and time-resolved photoluminescence (TRPL) spectra. Additionally, stability tests show an enhanced stability under ambient conditions for ZnP-modified SWCNTs compared to the reference device, which is attributed to the higher hydrophobicity introduced by the presence of CNMs, as shown in water-contact angle measurements.

Results and discussion

Synthesis and characterization of hybrid CNMs

The synthesis of precursor functionalizing molecules intended for the covalent modification of CNM surfaces is depicted in Scheme S1 (SI). Thus, 4-azido-*N*,*N*-bis(4-methoxyphenyl)aniline (TPAOMe-N_3), zinc(II) 5-(*p*-azidophenyl)-10,15,20-tris(4-(bis(4-methoxyphenyl)amino))-porphyrin (ZnP), and palladium(II)-5-(*p*-azidophenyl)-10,15,20-tris(4-(bis(4-methoxyphenyl)amino))-porphyrin (PdP) were prepared based on adapted procedures from the literature (see the SI for experimental details). Likewise, Fig. 1 illustrates the schematic representation of the synthetic preparation of p-type hybrid CNMs. A [2 + 1] nitrene cycloaddition was used to covalently modify SWCNTs and CNHs. In short, the reaction was carried out by combining the different CNMs with the previously described azido derivatives TPAOMe-N_3, ZnP-N_3, and PdP-N_3, and heating the mixture at 70 °C for 72 hours. The modified CNMs were then purified using standard washing, filtration, and sonication work-up, yielding the desired products.

The resulting p-doped modified CNMs were then subjected to different characterization techniques to confirm their successful covalent modification and to investigate their optoelectronic characteristics. Thermogravimetric analysis (TGA) was performed to confirm the presence of functional groups anchored to the surface of the different hybrid materials, based on the weight loss pattern of the functionalized CNMs compared to the pristine counterparts. Fig. S1 (SI) shows the characteristic weight loss of functionalized CNMs at 650 °C for **CNH-TPAOMe** and **SWCNT-TPAOMe**, and at 700 °C for **SWCNT-ZnP** and **SWCNT-PdP**, in comparison to their respective pristine nanomaterials, assuming that the TPA and porphyrin derivatives were completely removed from the CNM's surfaces at these temperatures. The corrected weight loss percentages for the pristine and the functionalized materials are presented in Table S1 (see the SI for more details). Considering the weight loss percentages of the new hybrid materials, the functional group coverage (FGC) and the functionalization degree (FD, μmol g^{-1} CNM) for each hybrid were estimated according to eqn (S1) and (S2) provided in the SI.[30–32] The additional weight loss (Wt_{Add}) observed for the functionalized CNMs are attributed to the decomposition of the TPAOMe and porphyrin ZnP and PdP derivatives covalently attached to the surface of CNMs. The clear increase in FGC observed in the functionalized materials confirms the successful formation of the targeted hybrid systems. X-ray photoelectron spectroscopy (XPS) was performed on both pristine and functionalized CNMs to investigate the surface chemical composition and confirm successful

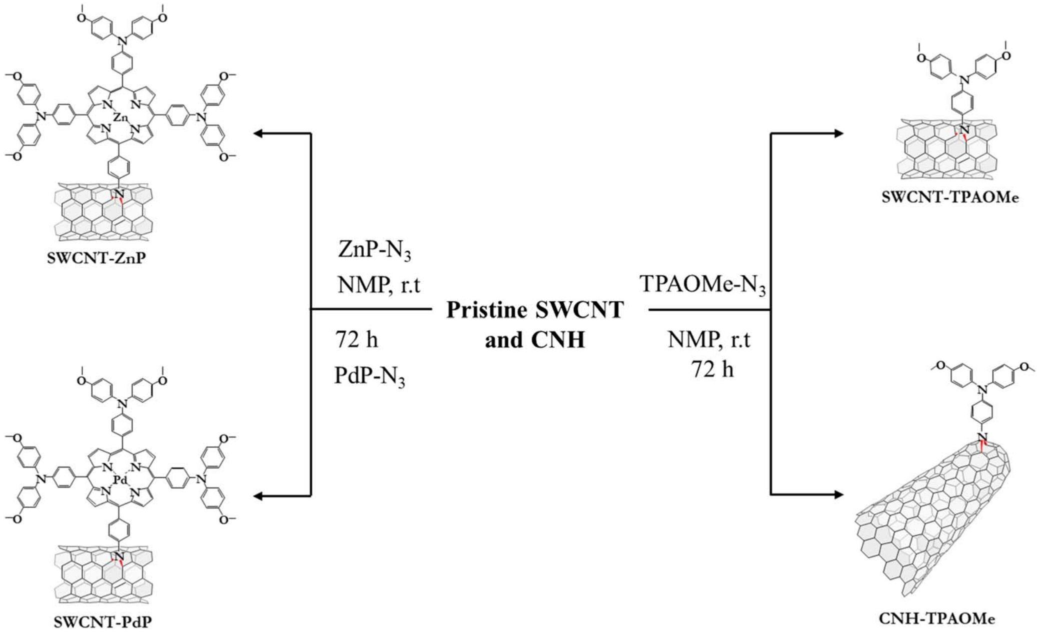

Fig. 1 Synthetic pathways for the preparation of **SWCNT-TPAOMe**, **CNH-TPAOMe**, **SWCNT-ZnP**, and **SWCNT-PdP**.

functionalization. Atomic percentages of each chemical element for the hybrid materials are collected in Table S2 and the XPS spectra are collected in Fig. S2 to S4. The spectra of both pristine CNHs and SWCNTs are characterized by the presence of carbon (C 1s) and oxygen (O 1s). However, as shown in Fig. S2a–S4a, the XPS spectra of the hybrid materials reveal a new peak at ~400.0 eV, typically assigned to the presence of nitrogen (N 1s).[33] In the case of TPA-OMe functionalized CNMs, the high-resolution N1s spectra can be fitted into two peaks at ~399.6 and ~400.0 eV, attributed to the presence of two distinct nitrogen species (Fig. S2b and S3b). The minor component corresponds to the nitrogen atoms present in the TPAOMe chemical structure, while the second one is associated with the nitrogen-containing aziridine open-ring configuration in functionalized CNMs.[24] This observation clearly verifies the successful anchorage of the TPA derivatives *via* aziridine-ring formation in **SWCNT-TPAOMe** and **CNH-TPAOMe**.

On the other hand, the spectra of **SWCNT-ZnP** and **SWCNT-PdP** reveal the presence of $Zn2p_{3/2}$ (~1023.0 eV) and $Pd3d_{5/2}$ (~338.1 eV) (Fig. S4b and c), confirming the successful incorporation of the porphyrin derivatives onto the surface of the CNMs.[34,35] As in the previous case, the high-resolution N 1s spectra of **SWCNT-ZnP** and **SWCNT-PdP** reveal the presence of multiple nitrogen components due to structural differences (Fig. S4d). In both cases, the N 1s signal can be fitted into three peaks: the first one at ~398.0 eV, assigned to nitrogen-containing open structures in functionalized nanotubes,[36] the second at ~399.5 eV, attributed to the nitrogen atoms of the metalloporphyrin macrocycle, and the third peak at ~400.3 eV, corresponding to the nitrogen of the TPAOMe moieties.[34,35] The XPS spectra also reveal an increased atomic percentage of oxygen in the functionalized samples compared to the pristine nanomaterials. The high-resolution O 1s spectrum of CNH derivatives exhibits two components at ~532.0 and 533.0 eV, corresponding to O=C and O–C surface groups, respectively (Fig. S2c).[37,38] A similar trend is observed for SWCNT derivatives (Fig. S3c, S4e, and S4f), where the deconvolution of the O 1s spectrum reveals two peaks at ~530.5 and 532.6 eV, assigned to O=C and O–C, respectively.[39] However, in the functionalized samples, the intensity of the O–C peak increases when compared to the pristine ones, likely due to the covalent introduction of oxygen-containing functional groups ($C–O–CH_3$) over the CNM surface after functionalization.

The Raman spectra of the different samples are shown in Fig. 2a–c, and the Raman data are collected in Table S3. As observed, after the covalent modification, the G band shifts to higher frequencies by 6, 4, 2, and 2 cm^{-1} for **CNH-TPAOMe**, **SWCNT-TPAOMe**, **SWCNT-ZnP**, and **SWCNT-PdP**, respectively. The observed spectral shifts confirm a p-type doping effect of the attached azido derivatives on CNMs in all cases.[40] This indicates an increment in hole carrier density, thereby enhancing the hole-transporting properties of the CNMs after the functionalization approach.[24] The I_D/I_G ratio is also a crucial parameter for evaluating the effects of covalent functionalization on the π-conjugated structure of the CNMs.[41] Complete statistical analysis of intensity ratios I_D/I_G and the D and G band positions of the Raman average spectra for the new hybrid materials are shown in Fig. S5 to S8. As observed, no increment in the D band was detected across extended regions of the sample following the functionalization process, confirming the preservation of the π-conjugated structure in the final hybrid materials. The consistent results obtained across different sample areas further support the reliability of the Raman data (Table S3).

UV-vis absorption spectra were recorded in *N*-methyl-2-pyrrolidone (NMP) for all samples (Fig. S9), a solvent well-suited

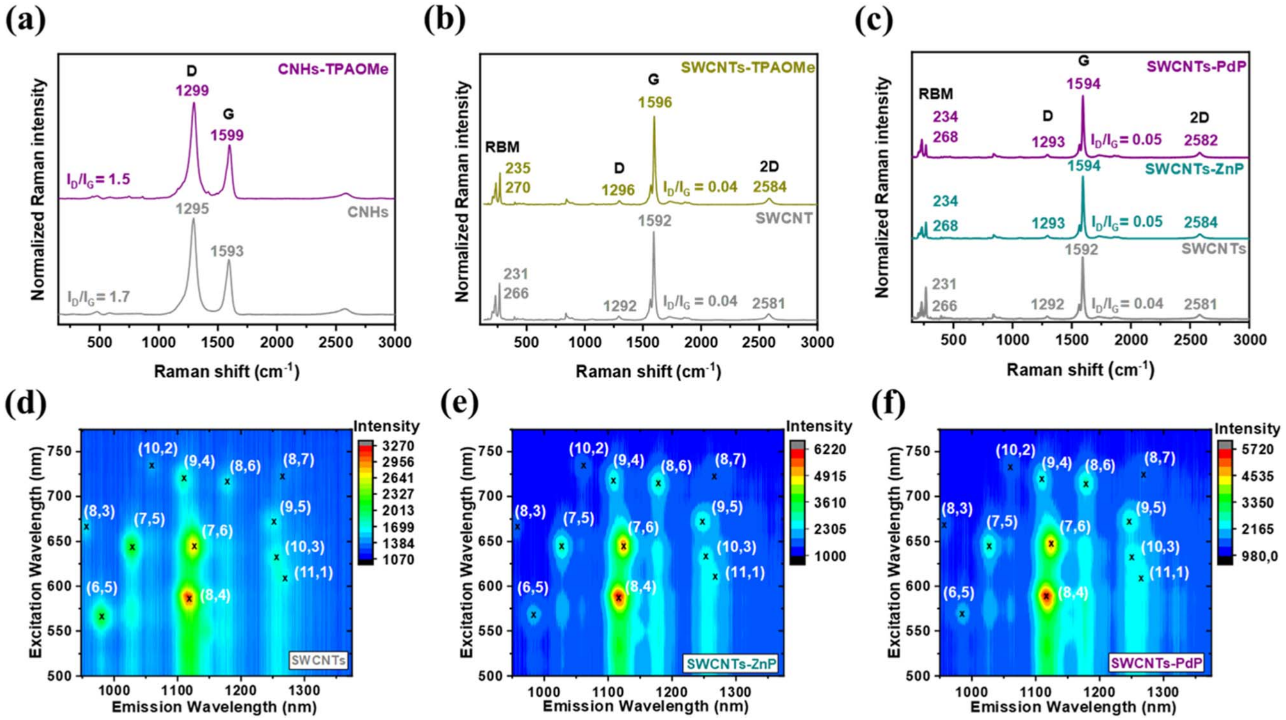

Fig. 2 Raman spectra for: (a) pristine CNHs compared to **CNH-TPAOMe**; (b) pristine SWCNTs compared to **SWCNT-TPAOMe**; and (c) pristine SWCNTs compared to **SWCNT-ZnP** and **SWCNT-PdP** (λ_{exc} = 785 nm). PLE maps for: (d) pristine SWCNTs, (e) **SWCNT-ZnP**, and (f) **SWCNT-PdP** recorded in Milli-Q grade water containing 10 wt% of dodecylbenzene sulfonate (SDBS) as a surfactant at room temperature. The (*n*, *m*) indices specify the SWCNT species associated with each emission spot.

for such measurements in CNMs due to its excellent dispersing ability.[42] Because of their non-uniform size and shape, the UV-vis spectra of pristine CNHs and **CNH-TPAOMe** were featureless (Fig. S9a). Furthermore, due to the absorption of TPA derivatives occurring near the cut-off wavelength of NMP, no significant differences were observed in the UV-vis spectra of the TPA-functionalized hybrid materials (Fig. S9a and S9b). On the other hand, the UV-vis absorption spectra of porphyrin **3** and **ZnP** registered in NMP displayed the characteristic Soret bands at 414 and 442 nm, respectively (Fig. S9c). It is important to note that **PdP** is highly unstable and decomposes rapidly, making its characterization particularly difficult by UV-vis spectroscopy and hampering the comparison in this case. In the UV region between 400 and 500 nm, corresponding to the Soret bands of the porphyrins, both **SWCNT-ZnP** and **SWCNT-PdP** exhibit a slight enhancement in absorbance intensity, indicative of successful functionalization. In particular, for **SWCNT-ZnP**, the Soret band is broadened and reveals a red shift of 4 nm, suggesting the presence of electronic interactions between the nanotubes and the electroactive porphyrin derivatives in the ground state.[34,35] Furthermore, UV-vis spectroscopy can also be useful for analysing the electrical disruption of the π-conjugated structure in SWCNTs.[43] In general, the formation of sp^3 C atoms disrupts the translational symmetry and alters the electronic structure of the SWCNTs, attenuating the van Hove singularities. The absorption spectra of **SWCNT-TPAOMe**, **SWCNT-ZnP**, and **SWCNT-PdP** reveal the characteristic van Hove singularities of pristine SWCNTs that remain comparable in the functionalized samples relative to the pristine forms. This confirms that the π-conjugation of the SWCNT network is preserved after the covalent functionalization process, as also suggested by the Raman spectroscopy results.

Photoluminescence excitation (PLE) intensity maps were recorded for the pristine SWNCTs, **SWCNT-ZnP**, and **SWCNT-PdP** in an aqueous solution of dodecylbenzene sulfonate (SDBS) at room temperature (Fig. 2d–f). It is well known that functionalization typically quenches photoluminescence in this type of materials due to the disruption of the π-conjugated system that alters the density of states (DOS) introducing non-recombination pathways. In the PLE spectrum of pristine SWCNTs (Fig. 2d), the semiconducting (8, 4) and (7, 6) chiralities are the most prominent species. Interestingly, after the covalent functionalization process, a slight increment in the light emission was observed for both (7, 6) and (8, 4) SWCNTs, which could be attributed to alterations of the electronic states of the nanotubes in the presence of porphyrin moieties, leading to increased photoluminescence.[35,44] However, no quenching or shifts of the bright spots were observed in the functionalized materials, indicating the preservation of the π-conjugated network in accordance with the previous results.[35,45,46]

The structures of **SWCNT-TPAOMe** and **SWCNT-ZnP** systems were optimized at the density functional theory (DFT) level of theory using the CAM-B3LYP functional,[47] the def2-svp basis set,[48] and the D4 dispersion correction scheme[49–51] as representative examples of the chemically functionalized CNMs studied in this work (see full computational details in the SI).

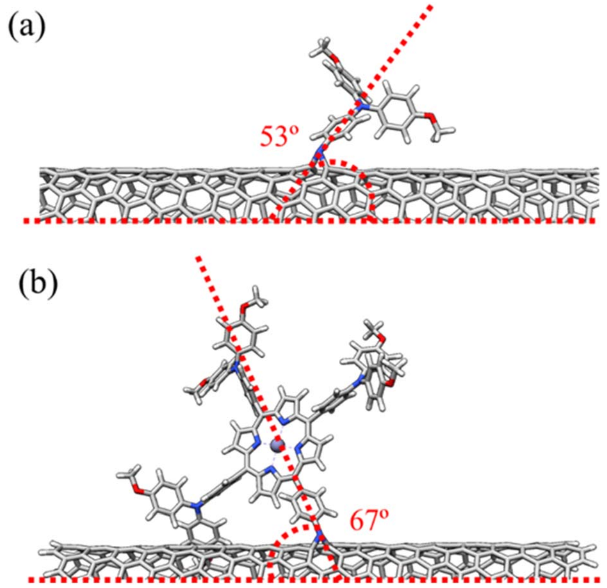

Fig. 3 CAM-B3LYP/def2-svp minimum-energy structures calculated for **SWCNT-TPAOMe** (a) and **SWCNT-ZnP** (b). The angles marked in dashed red lines correspond to those formed between the N–N long axis of the substituent groups and the long axis of the nanotube skeleton. Atom color code: C (gray), N (blue), H (white), O (red), and Zn (purple, sphere).

Both TPAOMe and ZnP substituents form an angle over 50° with the long axis of the nanotube (53° and 67°, respectively, as shown in Fig. 3). The large size of the porphyrin group allows for intramolecular π–π interactions between the peripheral phenyl rings and the C=C framework of the nanotube. As suggested by the experimental data, the TPAOMe and ZnP moieties induce only minor modifications on the C–C π-conjugated framework of the nanotube, with bond length distortions lower than 0.1 Å in the environment of the aziridine open ring (Fig. S10). The root mean square deviation (RMSD) for the coordinates of the C atoms compared to the pristine nanotubes is 0.03 Å for both **SWCNT-TPAOMe** and **SWCNT-ZnP**, the main distortion corresponding to a 0.4 Å out-of-plane displacement of one of the substituted C atoms.

Perovskite solar cell device fabrication and characterization

Fig. S15 shows the schematic illustration of the fabrication of PSC devices incorporating the described CNMs as additives for spiro-OMeTAD. Planar solar cell devices with the architecture FTO/SnO_2/$FA_{0.3}MA_{0.7}PbI_3$/spiro-OMeTAD-CNMs/Au were fabricated through a simple and cost-effective spin-coating method. The SnO_2 electron-transporting layer (ETL) was first deposited on the glass/FTO substrate, followed by coating with the perovskite layer using a one-step anti-solvent method. Then, spiro-OMeTAD doped with CNMs was deposited over the perovskite layer. Finally, Au electrodes were deposited through thermal evaporation (see details in the SI). For all devices, spiro-OMeTAD was doped with Li-TFSI, tBP, and FK-209. The devices fabricated with spiro-OMeTAD without any CNM additive will be termed as w/o CNMs or pristine spiro-OMeTAD devices, and the devices fabricated with CNM-containing spiro-OMeTAD will be termed as **SWCNT-TPAOMe**, **SWCNT-ZnP**, **SWCNT-PdP**, and **CNH-TPAOMe** devices.

Fig. 4a shows the structure of the PSC devices, and the cross-sectional SEM image of devices with **SWCNT-ZnP** and pristine spiro-OMeTAD are displayed in Fig. 4b and S16, respectively. It shows a multilayer structure, which is vital for enhancing charge carrier dynamics.[52–54] Fig. 4c illustrates that devices treated with **SWCNT-ZnP** show a uniform pinhole-free surface of spiro-OMeTAD, which is also beneficial for the transportation of hole charge carriers. In Fig. 4c, some white spots appear on the surface of the HTL, which might come from the aggregation of CNMs on the surface of the spiro-OMeTAD treated with **SWCNT-ZnP**.[15,55–58] In contrast, devices fabricated without CNMs show the presence of pinholes on the surface of the spiro-OMeTAD as shown in Fig. S17a. To confirm this, a topographic AFM of the HTL layer (spiro-OMeTAD and **SWCNT-ZnP**-treated spiro-OMeTAD) was performed ($5 \times 5\ \mu m^2$, at a rate of 0.5 Hz). The pristine spiro-OMeTAD HTL layer shows a RMS roughness of 4.51 nm, showing clear pinholes on the surface (see Fig. S18a). The **SWCNT-ZnP**-treated spiro-OMeTAD layer shows a RMS roughness of 2.86 nm with the disappearance of the pinholes (see Fig. S18b and Table S8 for their corresponding RMS and average roughness values). The different scan regions ($1 \times 1\ \mu m^2$) of both HTLs are shown in Fig. S19, and mean RMS roughness with standard error is shown in Table S9. Existing studies show that pinholes in the HTL layer locally remove the hole-selective barrier and can enable direct perovskite/metal contact. This creates leakage paths (low R_{sh}) and enhanced recombination, which suppress V_{OC} and FF of the devices.[59] This uniform surface with lower roughness of the **SWCNT-ZnP**-treated films show stronger interfacial contact which enables efficient hole extraction and decreases recombination.[60] Therefore, devices fabricated with **SWCNT-ZnP** enhance the surface morphology of the spiro-OMeTAD film and improve the device performance. Similar to devices without CNMs, the surface morphology of **SWCNT-PdP** shows multiple pinholes (Fig. S17b), which limit the device performance. In contrast, **SWCNT-TPAOMe** shows a uniform and pinhole-free film (Fig. S17c) that facilitates charge transportation, thus resulting in improved device performance when compared to spiro-OMeTAD.

To gain insight of the energy match between the HTM-modified layers and the perovskite material, we performed ultraviolet photoelectron spectroscopy (UPS) of all the layers incorporated in the PSC devices as shown in Fig. S20. Spiro-OMeTAD treated with CNMs adjusts the HOMO, thus facilitating the hole transfer to the corresponding HTL (see the schematic in Fig. 5a). This decrease in energy loss during the charge carrier transportation along the perovskite–HTL interface is an important factor for enhancing PSC device performance. The HOMO changes from −5.24 eV for the w/o CNM layer to −5.31 eV for the **SWCNT-ZnP** HTM layer. The addition of CNMs into spiro-OMeTAD moves the HOMO closer to the perovskite VBM, which enhances the charge carrier transportation and decreases the charge carrier loss, thus resulting in an enhanced device performance.

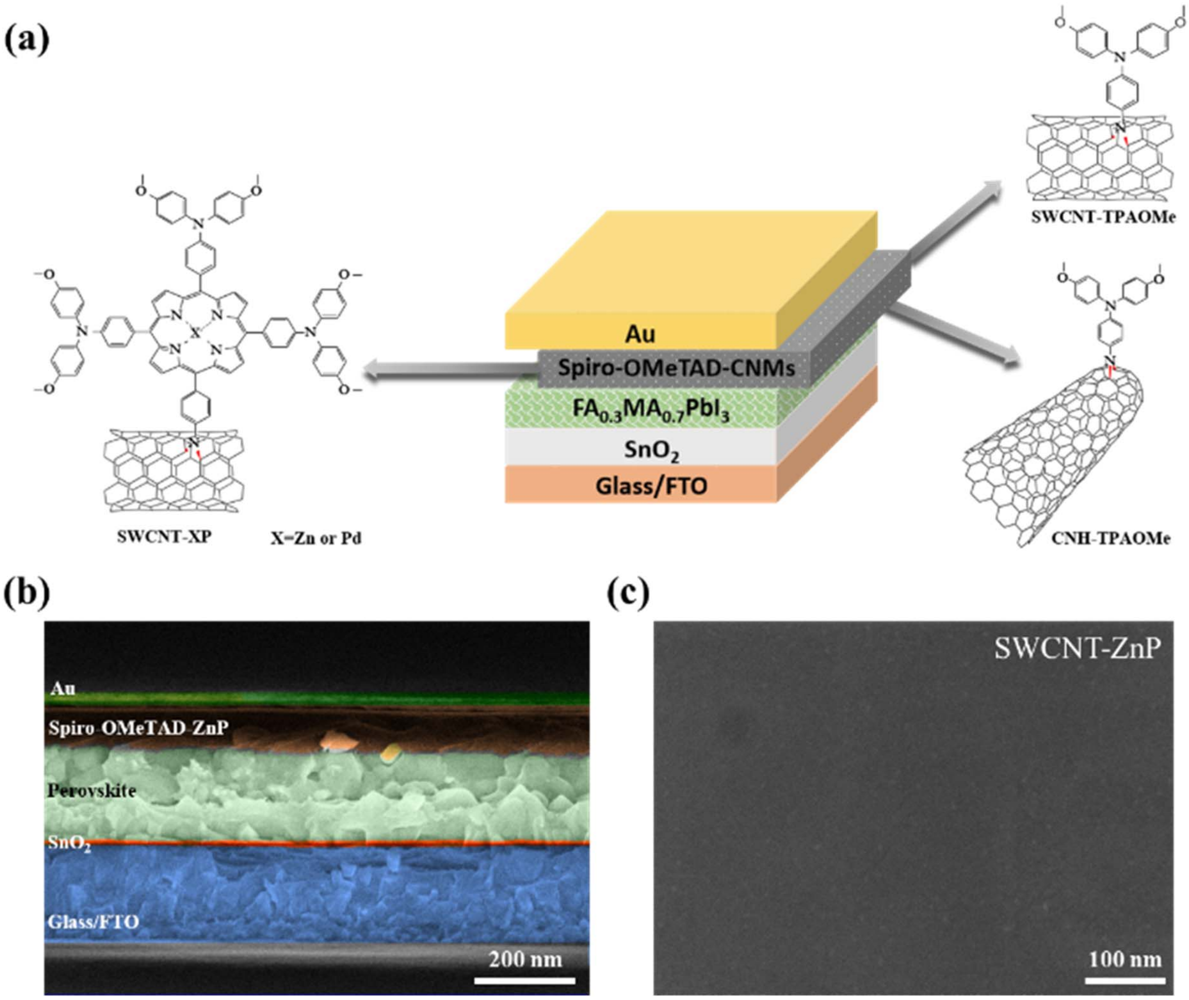

Fig. 4 (a) Device's structure with incorporated p-functionalized CNMs. (b) Cross-sectional SEM image of the device. (c) Planar SEM image of spiro-OMeTAD treated with **SWCNT-ZnP**.

Fig. 5b represents the current density–voltage (J–V) characteristics of PSC devices with and without CNMs. The devices were simulated under AM 1.5G illumination. The respective device parameters are listed in Table 1. The pristine (w/o CNMs) devices show a maximum power conversion efficiency (PCE) of 18.01%, a short-circuit current density (J_{SC}) of 23.63 mA cm^{-2}, an open-circuit voltage (V_{OC}) of 1.03 V, and a fill factor (FF) of 73.76%. The devices treated with functionalized **SWCNT-ZnP** show notably enhanced PCE of 19.76%, J_{SC} of 23.74 mA cm^{-2}, V_{OC} of 1.06 V, and FF of 78.50%. This enhancement in the performance of **SWCNT-ZnP**-treated devices corresponds to the better energy level alignment and uniform morphology,[61,62] which makes charge carrier transportation faster, as verified from the UPS analysis discussed above. This is also consistent with the Raman analysis. Our results strongly suggest that porphyrin-functionalized CNMs are potential candidates for doping spiro-OMeTAD-based HTLs.

The devices treated with **SWCNT-TPAOMe** show a maximum PCE of 18.96%, J_{SC} of 23.57 mA cm^{-2}, V_{OC} of 1.03 V, and FF of 77.97%. They show enhanced performance compared to devices w/o CNMs, while lower than the devices treated with **SWCNT-ZnP**.[24] Conversely, the devices fabricated with **SWCNT-PdP** show a decrease in the overall performance compared to pristine devices, as shown in Table 1. The lower performance of devices fabricated with functionalized palladium porphyrins can be attributed to the bad surface morphology and uneven energy levels, which generate energy losses across the interfaces, causing decreased values for all the photovoltaic parameters, including PCE. This lower performance of the devices can also be due to the bad dispersion of **SWCNT-PdP** into spiro-OMeTAD, which disrupts the charge carrier transportation and degrades device performance. The devices fabricated with **CNH-TPAOMe** show almost similar device characteristics as pristine devices, which reveals that **CNH-TPAOMe** did not significantly influence the transportation of charge carriers. This indicates that the behaviour of such materials has little or no impact on the hole mobility of the HTMs.

The external quantum efficiency (EQE) spectra also confirm the deviation in PSC device current densities, as illustrated in Fig. 5c. EQE spectra measured in the wide spectrum of 300–850 nm are consistent with the J–V curves in Fig. 5b and also with the absorption spectra shown in Fig. S21a, while absorption

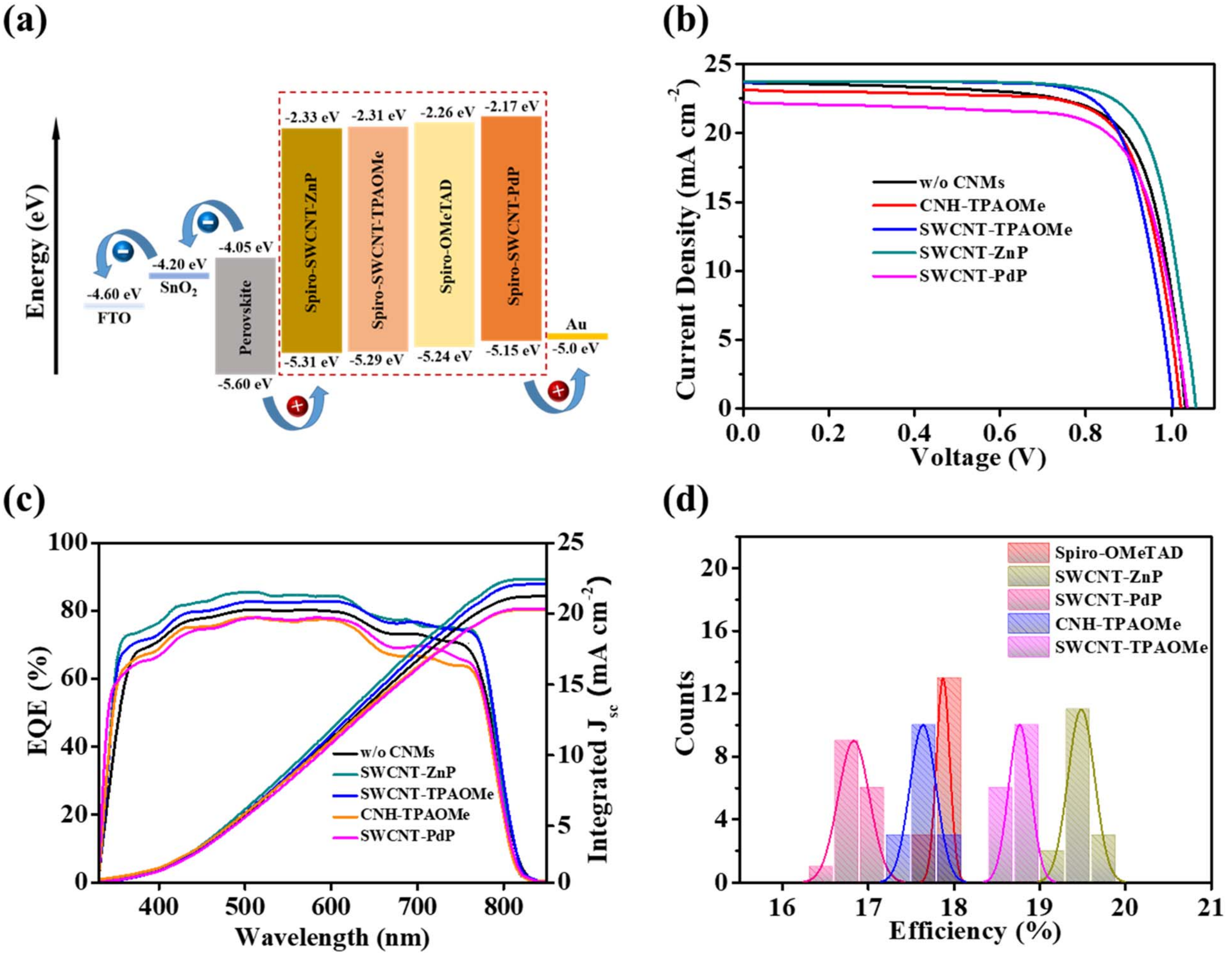

Fig. 5 (a) Energy level diagram of PSCs with and without CNMs. (b) J–V characteristics of PSC devices with and without CNMs. (c) External Quantum Efficiency (EQE) spectra of all devices with corresponding integrated J_{SC}. (d) Efficiency distribution histogram of PSC devices with and without CNMs.

spectra of spiro-OMeTAD incorporating functionalized CNMs are shown in Fig. S21b. This depicts the excellent capability of our devices to convert light energy into electrical current. It also confirms that the incorporation of functionalized CNMs into spiro-OMeTAD films enhances the short circuit current densities and improves the integrated J_{SC} of devices fabricated with **SWCNT-ZnP** compared to the rest of the CNMs. The integrated current densities obtained from the EQE spectra are gathered in Table 1. However, these values are slightly lower than the values obtained from the J–V curve. A batch of 15 devices were fabricated to study the reproducibility and viability of our devices, as shown in Fig. 5d histogram. The deviation in efficiency of spiro-OMeTAD devices ranges from 17.75 to 18.01% with a mean value of 17.87%, while devices fabricated with **SWCNT-ZnP** show deviations from 19.15 to 19.76% with a mean value of 19.53%. This highlights the excellent reproducibility of the PSC devices. Additionally, statistical distribution of all the PSC devices with V_{OC}, J_{SC}, PCE, and FF are shown in Fig. S23 (device parameters with average values and standard errors are collected in Table S12).

To investigate the effect of the substituent group on the energy levels of the SWCNTs, the CAM-B3LYP-D4/def2-svp

Table 1 Best performing PSC device parameters and integrated J_{SC} for each CNM

HTMs	V_{OC} (V)	J_{SC} (mA cm^{-2})	FF (%)	PCE (%)	Integrated J_{SC} (mA cm^{-2})
Spiro-OMeTAD (w/o CNMs)	1.03	23.63	73.76	18.01	21.62
CNH-TPAOMe	1.02	23.07	75.87	17.91	20.27
SWCNT-TPAOMe	1.03	23.57	77.97	18.96	22.10
SWCNT-PdP	1.03	22.20	74.23	17.11	20.36
SWCNT-ZnP	1.06	23.74	78.50	19.76	22.84

molecular orbitals calculated for **SWCNT-TPAOMe** and **SWCNT-ZnP** were compared to those of the pristine (8, 4) SWCNTs. As shown in Fig. S11, our reference HOMO and LUMO orbitals resemble those obtained for the pristine nanotubes, with no significant contribution of the substituent groups (see the SI for details). This result aligns with the conservation of the sp^2 network of the carbon nanotubes upon functionalization. As detailed in Table S4, the functionalization of the (8, 4) SWCNTs with TPAOMe and **ZnP** increases the energy of the HOMO, making the CNTs better electron donor, and induces a narrowing of the HOMO–LUMO energy gap changing from 2.77 eV for the pristine SWCNTs to 2.35 eV for **SWCNT-ZnP**.

The effect of doping spiro-OMeTAD with functionalized nanotubes on the charge transport properties and the electronic energy level alignment with the perovskite was investigated by analyzing the electronic properties of the most strongly interacting molecular clusters resulting from spiro-OMeTAD aggregation on the functionalized nanotubes obtained from the iterative docking/re-optimization procedure (see the SI for computational details). For both **SWCNT-TPAOMe** and **SWCNT-ZnP**, the first interacting layer consists of five molecules of spiro-OMeTAD supramolecularly bounded to the nanotube skeleton by π–π interactions between the nanotube and the peripheral phenyl rings and fluorene core of spiro-OMeTAD but rather weak interactions with the nanotube substituents (see Fig. 6 for **SWCNT-TPAOMe** and Fig. S12 for **SWCNT-ZnP**, respectively). Interestingly, the coordination of spiro-OMeTAD to the functionalized nanotubes has minimal influence on the delocalization of the reference HOMO and LUMO orbitals, which remain predominantly localized on the nanotube framework (Fig. S13 and S14). The orbitals are, however, shifted to higher energies (up to ∼0.3 eV) upon aggregation with the electron-donor spiro-OMeTAD molecules for both **SWCNT-TPAOMe** and **SWCNT-ZnP** (Tables S5 and S6).

The space-charge-limited current (SCLC) method was used to find the trap density of the materials, which further verifies the *J–V* behaviour of pristine and **SWCNT-ZnP** devices. The devices fabricated with FTO/NiO_x + 5%Cu/perovskite/spiro-OMeTAD/Au and FTO/NiO_x + 5%Cu/perovskite/spiro-OMeTAD-**SWCNT-ZnP**/Au architecture (Fig. 7a inset) show the *J–V* curve of hole-only devices. The *J–V* characteristics of these hole-only devices were classified into three types of region, as shown in Fig. 7a, according to the slope (m): the ohmic region ($m \approx 1$), which is in the low injection regime, a trap-filled limited (TFL) region ($m > 3$), and a space charge limited current regime (Child, $m \approx 2$). V_{TFL} was measured using a two-line intersection method, and the estimated V_{TFL} is the intersection between the ohmic region and the TFL region, which is consistent with the conventional SCLC literature.[64–66] Trap densities (N_t) were calculated through eqn (S3) as described in the SI. The mean V_{TFL} values extracted for pristine spiro-OMeTAD and **SWCNT-ZnP** devices are 0.718 ± 0.0257 V and 0.625 ± 0.0112 V, respectively, while the calculated N_t values are 1.01 ± 0.0356 ($\times 10^{16}$ cm^{-3}) and 0.887 ± 0.0161 ($\times 10^{16}$ cm^{-3}), respectively. Fig. S24 shows the statistical

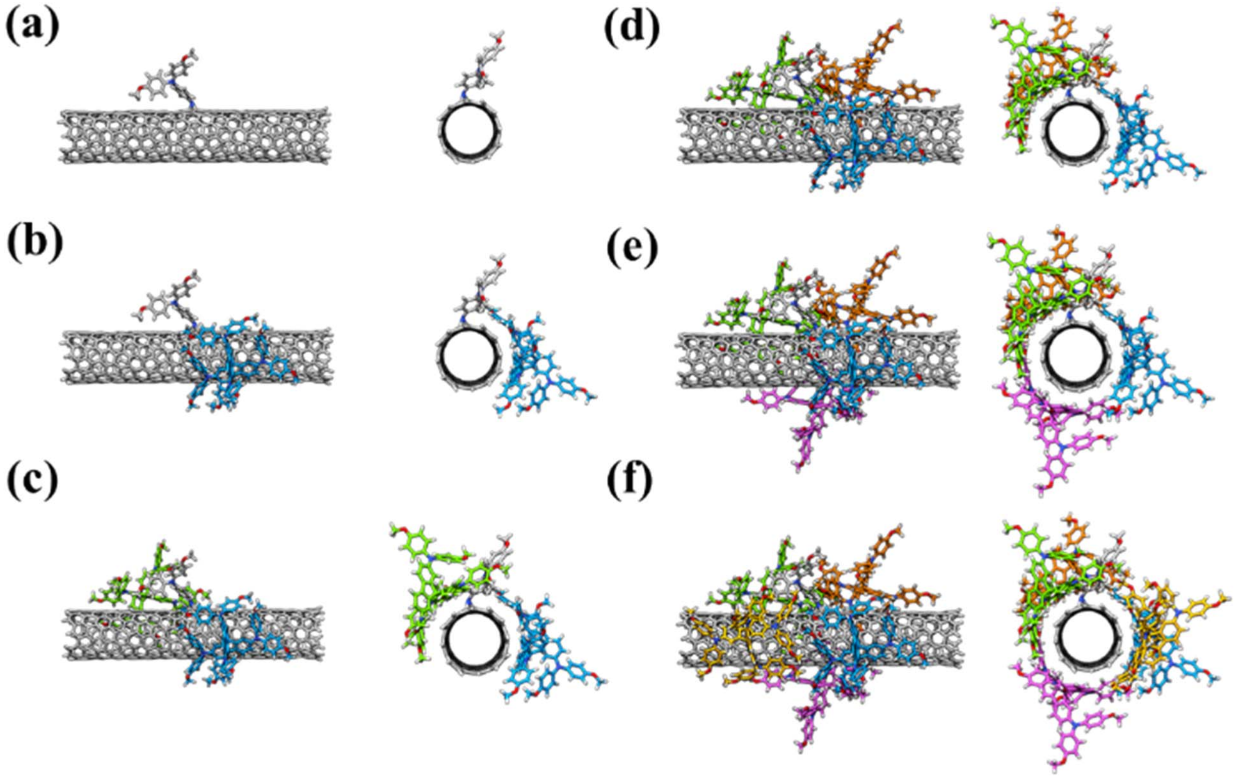

Fig. 6 Iterative aiSS[63] docking procedure for the coordination of up to 5 spiro-OMeTAD molecules to (a) pristine **SWCNT-TPAOMe**. The number of aggregated spiro-OMeTAD molecules is increases from 0 (a) to 5 (f) respectively, and each molecule is highlighted by using C atoms of different colors (**SWCNT-TPAOMe** C atoms are shown in grey color).

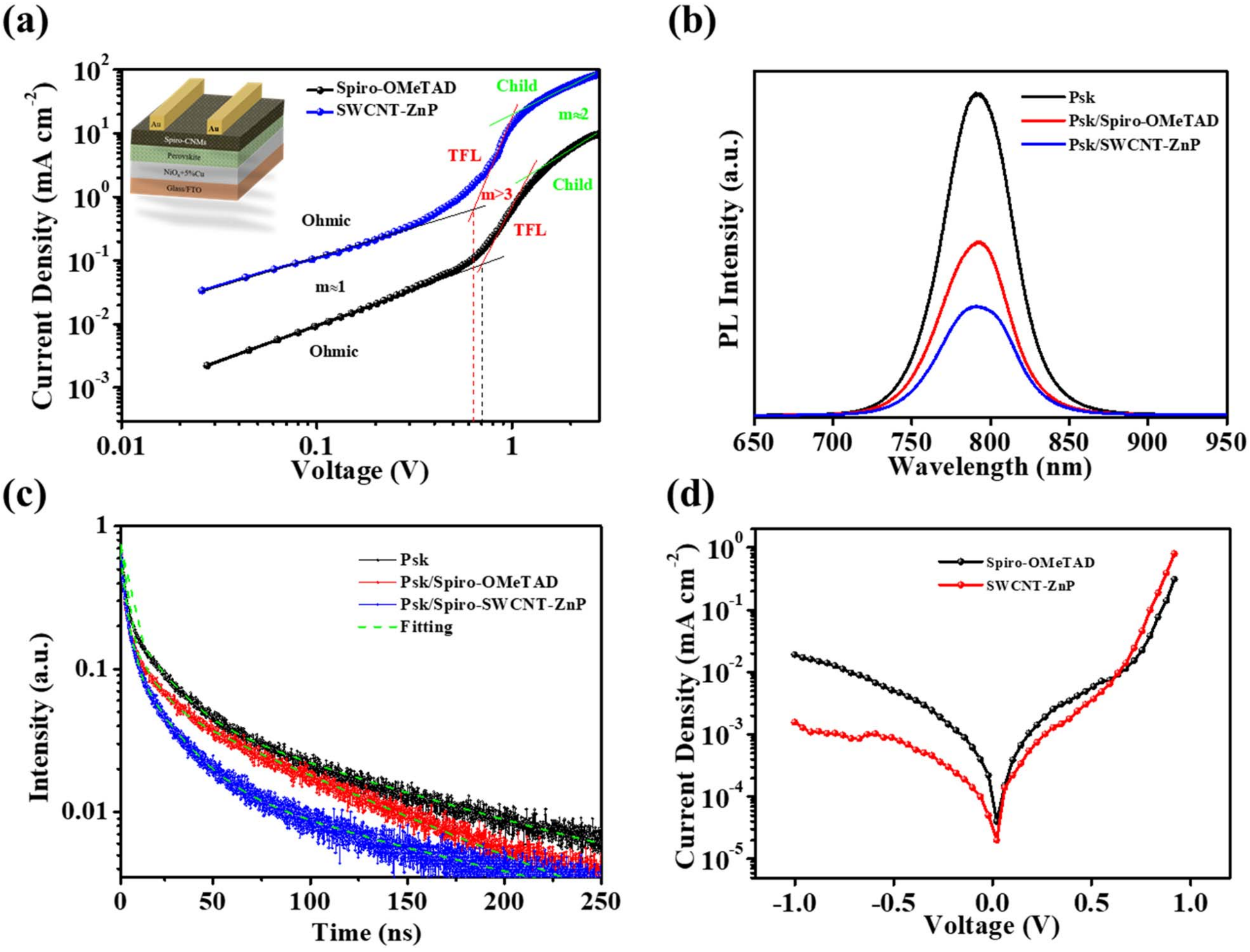

Fig. 7 (a) Dark *J*–*V* characteristics of hole-only devices with and without CNMs. (b) PL spectra and (c) TRPL spectra of perovskite (psk), psk/spiro-OMeTAD, and psk/**spiro-SWCNT-ZnP** films. (d) Dark *J*–*V* characteristics of PSCs with pristine spiro-OMeTAD and spiro-OMeTAD treated with SWCNT-ZnP.

distribution of V_{TFL} and N_{t} to see the error and repeatability of devices (5 sweeps). These results show that addition of **SWCNT-ZnP** to spiro-OMeTAD decreases the trap densities, which enhances the charge carrier transportation and reduces recombination, resulting in enhanced device performance.[67]

The hole mobility of the devices was calculated through the SCLC method to further verify the effect of **SWCNT-ZnP** on charge carrier transportation. The mobilities were calculated by using the Mott–Gurney law (eqn (S4) in the SI). The estimated mobilities for spiro-OMeTAD and **SWCNT-ZnP** are 3.70×10^{-3} and 4.99×10^{-3} cm^2 V^{-1} s^{-1}, respectively. Charge extraction in pristine spiro-OMeTAD devices is limited by the low mobility of the photogenerated charges inside the spiro-OMeTAD layer, which results in lower device performance.[68] Therefore, the increase in hole mobility of the carriers with the addition of **SWCNT-ZnP** might be attributed to the suitable HOMO energy levels and uniform morphology of the resulting HTL, which increases current density, and improves the FF and efficiency of the devices, consistent with previous observations.[69] The interaction between **SWCNT-ZnP** and spiro-OMeTAD effectively passivates the surface defects, which also contributes to increased hole mobility and enhanced hole extraction. The mean trap density and mobility values of pristine spiro-OMeTAD and **SWCNT-ZnP** treated devices are given in Table S13.

Recently, we theoretically investigated and rationalized the impact of morphology and temperature on the hole mobility of spiro-OMeTAD in both amorphous and crystalline phases, as it was proved to increase upon crystallization.[70,71] In the framework of the Marcus theory, the hole and electron mobilities within molecular pairs increase if the electronic coupling between the HOMOs (hole transport) or the LUMOs (electron transport) is enhanced. Our previous results demonstrated that if low ordering is assumed, the electronic coupling distribution within molecular pairs of spiro-OMeTAD molecules is rather narrow, with values in the range from −5 to 5 meV.[72] To investigate the effect of doping spiro-OMeTAD with functionalized nanotubes on the hole mobilities, we calculated the electronic coupling between the reference HOMO of the chemically substituted SWCNTs and the HOMO of the respective spiro-OMeTAD molecules successively aggregated using a docking procedure. For both **SWCNT-TPAOMe** and **SWCNT-ZnP**, significantly high electronic couplings up to almost 40 meV are obtained (Table S7) due to the delocalization of the nanotube HOMO over the carbon conjugated network, offering a platform on which the spiro-OMeTAD molecules aggregate to maximize the π–π intermolecular interactions. These high electronic couplings, together with the small cation reorganization energies computed for **SWCNT-TPAOMe** (0.04 eV) and **SWCNT-ZnP** (0.05 eV) compared to that for spiro-OMeTAD (0.45 eV), enhance hole transfer along the doped films. Remarkably, the GFN2-xTB[73] interaction energy between the most interacting spiro-OMeTAD molecule and the pristine SWCNTs (-54.76 kcal mol^{-1}) or the functionalized **SWCNT-TPAOMe** (-55.05 kcal mol^{-1}), and **SWCNT-ZnP** (-59.60 kcal mol^{-1}) are larger than within the two molecules forming the most stable spiro-OMeTAD dimer (-48.45 kcal mol^{-1}). This suggests that the aggregation of spiro-OMeTAD with the nanotube is more efficient and, therefore, is preferred to that between spiro-OMeTAD molecules. The occurrence of this aggregation and the high electronic couplings between the spiro-OMeTAD molecules and the functionalized nanotube effectively contributes to increasing the charge transport in SWCNT-treated spiro-OMeTAD films.

Photoluminescence (PL) and time-resolved photoluminescence (TRPL) characterization studies were performed to study the relationship between charge carrier extraction and device performance (Fig. 7b and c). FTO substrates were used to deposit the films. The bare FTO/perovskite film shows an intense PL peak, which reveals that a large charge carrier recombination occurred without the HTL. Deposition of spiro-OMeTAD on the perovskite layer (FTO/perovskite/spiro-OMeTAD) quenched the PL peak intensity, demonstrating that extraction of holes takes place thus decreasing the charge carrier recombination and the light emission.[74] **SWCNT-ZnP**-treated films (FTO/perovskite/spiro-OMeTAD-**SWCNT-ZnP**) show further decrease in PL intensity because of the improved surface morphology and thus enhanced charge extraction. Therefore, the PL intensity of **SWCNT-ZnP**-treated films decreases compared to bare perovskite and pristine spiro-OMeTAD films. The PL spectra recorded for the rest of the CNMs (**SWCNT-PdP**, **SWCNT-TPAOMe**, and **CNH-TPAOMe**) (Fig. S25a) are in good agreement with the previous observations. The PL intensity of the perovskite, perovskite/**SWCNT-ZnP**, and the whole device (SnO_2/perovskite/**SWCNT-ZnP**) are shown in Fig. S25b. The quenching of PL intensities was further supported by TRPL. Charge carrier lifetimes of the corresponding films were obtained by biexponential decay,[75] (eqn (S5) in the SI). The bare perovskite film shows the highest lifetime of the charge carriers (134.82 ns), while pristine spiro-OMeTAD films (FTO/perovskite/spiro-OMeTAD) show a lower carrier lifetime (56.71 ns), and the spiro-OMeTAD film treated with **SWCNT-ZnP** presents the lowest lifetime of the charge carriers (37.12 ns). These carrier lifetimes are consistent with the PL quenching phenomena. The lowest carrier lifetime of the treated HTLs is due to the enhanced charge extraction at the perovskite/HTL interface and the reduced energy barrier (in agreement with UPS results), leading to a more efficient hole transfer. Therefore, **SWCNT-ZnP**-treated devices depict a better charge extraction that leads to high mobility and enhanced PCE of the devices. **SWCNT-ZnP** treated films show slight increase in PL FWHM (≈2.4 nm), while TRPL reveals a substantially faster decay, consistent with efficient interfacial hole extraction,[76] which is the predominant effect. The small increase in FWHM likely reflects minor interfacial energetic disorder/tail states or halide distribution at the interface.[77–79] Calculated charge carrier lifetimes for spiro-OMeTAD films treated with **SWCNT-PdP**, **SWCNT-TPAOMe**, and **CNH-TPAOMe** were found to be 68.4, 40.62, and 53.23 ns, respectively, as shown in Fig. S26a. The TRPL of bare perovskite, perovskite/SWCNT-ZnP, and whole device (SnO_2/perovskite/**SWCNT-ZnP**) are shown in Fig. S26b. SnO_2/perovskite/**SWCNT-ZnP** shows fast TRPL decay compared to bare perovskite and perovskite/**SWCNT-ZnP**, which shows a fast photogenerated charge carrier separation and collection, resulting in enhanced device performance. The calculated charge carrier lifetimes of perovskite, perovskite/**SWCNT-ZnP**, and whole device (SnO_2/perovskite/**SWCNT-ZnP**) are 134.82, 37.12, and 26.90 ns, respectively. All the TRPL parameters with and without CNMs are listed in Table S14.

Fig. 7d depicts the dark *J*–*V* characteristic of the devices fabricated with pristine spiro-OMeTAD and **SWCNT-ZnP** treated spiro-OMeTAD. The devices treated with **SWNCT-ZnP** show lower values of dark current density compared to pristine spiro-OMeTAD devices. Furthermore, high dark current reduces the V_{OC} of the PSC devices, leading to a lowering of the PCE.[80,81] Therefore, treated devices suppress charge carrier recombination and improve the charge extraction at the perovskite/HTL interface, resulting in a decreased dark current and an improved V_{OC}. These results are consistent with the SCLC data calculated from charge carrier density and hole mobility.

One of the key parameters to characterize solar cell devices for commercialization is to determine the hysteresis of the devices. Trapping of charge carriers at interfaces and surface defects of films is specifically related to hysteresis and is detrimental for device performance.[82–84] Devices were analyzed in reverse and forward scan directions, as shown in Fig. S22. To calculate the hysteresis index (HI) (device parameters are gathered in Table S10). The resulting HI was calculated to be 0.034 for pristine spiro-OMeTAD, while devices treated with **SWCNT-ZnP** showed a reduced HI of 0.013, as shown in Table S11. This decrease in HI reveals a reduction in defects, resulting in improved mobility and enhanced charge extraction, which agrees with our previous TRPL, trap density, and SEM results.

A significant hurdle in the commercialization of PSCs is the stability of these devices. *J*–*V* stability measurements of devices fabricated with pristine spiro-OMeTAD and **SWCNT-ZnP** were conducted for 900 h under a relative humidity of 30–40%. The unencapsulated devices were aged at room temperature in an ambient environment. Fig. 8a shows that devices fabricated with pristine spiro-OMeTAD retain only 56% of their original PCE, while devices fabricated with **SWCNT-ZnP** retain 89% of their initial PCE. The incorporation of **SWCNT-ZnP** into spiro-OMeTAD improves the surface morphology of the HTL, which enhances the hydrophobicity and protects the device from degradation. Water contact angle measurements were also performed to further verify the hydrophobicity effect on the HTL (Fig. 8b, c and S27). Pristine spiro-OMeTAD-based devices

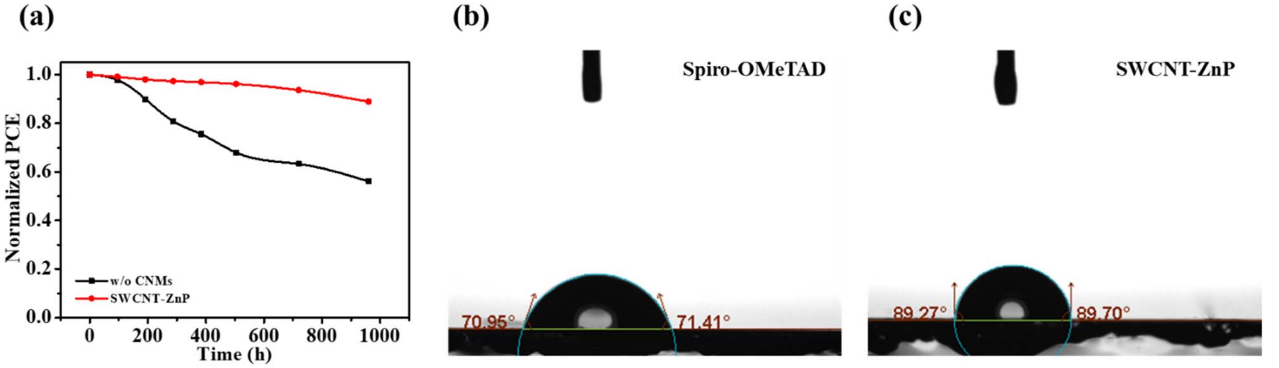

Fig. 8 (a) Long term stability of PSC devices with pristine spiro-OMeTAD and **SWCNT-ZnP**-treated spiro-OMeTAD. Water contact angle measurement of (b) spiro-OMeTAD and (c) **SWCNT-ZnP**-treated spiro-OMeTAD (both HTLs were deposited on the perovskite film).

showed a low contact angle (Fig. 8b), which, in addition to the presence of pinholes as discussed previously (Fig. S17a and S18a), leads to a solvent trapping effect, thus resulting in a low hydrophobicity. Therefore, both pinholes and the hydrophobic nature of the spiro HTL facilitate ion migration and drastically decrease the device stability.[62] The **SWCNT-ZnP**-treated devices show a higher contact angle (Fig. 8c), which is favourable for resisting moisture and slowing down the water penetration into the active layer in a humid environment. This high hydrophobicity, together with the uniform pinhole-free film previously shown in Fig. 4c and S18b, leads to a decrease in ion migration and enhances the stability of **SWCNT-ZnP**-treated devices, retaining up to 89% of its initial PCE value.

Conclusions

In conclusion, we present the successful functionalization of carbon nanomaterials, mainly carbon nanotubes (SWCNTs) and carbon nanohorns (CNHs), through [2 + 1] cycloaddition reactions with *p*-methoxytriphenylamine (TPA-OMe) and TPA-*meso*-substituted-porphyrins (Zn and Pd). A complete chemical and optoelectronic characterization is presented, confirming the precise functionalization of carbon nanostructures and its predicted properties. Theoretical calculations were performed to support the experimental properties of the new functionalized CNMs and their interaction with the reference hole-transporting material, spiro-OMeTAD. The incorporation of the functionalized SWCNTs and CNHs as an additive into the spiro-OMeTAD benchmark compound resulted in an improved energy alignment due to the energy shift of the spiro-OMeTAD and enhanced hole mobilities. Additionally, from SEM and AFM images, an improved morphology and contact interface of the perovskite/hole-transporting material (HTM) layer in the presence of the functionalized CNMs is observed, highlighting the case of Zn-porphyrin-SWCNTs (ZnP). As a consequence, the best-performing devices incorporating ZnP-functionalized SWCNT as an additive reached a maximum PCE of 19.8%, notably higher than that measured for the reference devices. Interestingly, the preliminary stability tests under dark storage and a relative humidity of 30–40% also show an improved stability when ZnP is incorporated into the spiro-OMeTAD solution, mainly attributed to the enhanced hydrophobicity of the layer determined from the water contact angle measurements. As a result, a notable effect is that introduction of functionalized CNMs into the spiro-OMeTAD layer results in adjusting the energy levels, enhancing the hole mobility and hydrophobicity, and improving the surface contact, leading to an improved performance in planar perovskite solar cells.

Author contributions

A. A.-K. and H. U. contributed equally to this work. E. O, F. L. and N. M. designed and supervised the project. J. U.-M., M. B. and J. C. advised on the research. H. U. and M. B. synthesized and characterized carbon nanomaterials. A. A.-K., S. A.-G. and J. U.-M. fabricated and characterized the solar devices and analyzed experimental data. M. P.-E. and J. C. performed the theoretical calculations. A. A.-K., H. U., J. U.-M and M. P.-E. wrote the manuscript. M. B., E. O., F. L. and N. M. revised and edited the manuscript. All the authors contributed to the discussion of the manuscript.

Conflicts of interest

There are no conflicts to declare.

Data availability

All (other) data needed to evaluate the conclusions in this work are presented in the manuscript or in the supplementary information (SI). Supplementary information is available. See DOI: **https://doi.org/10.1039/d5ta07147j**.

Acknowledgements

N. M., A. A.-K., J. U.-M. and S. A.-G. are grateful for the financial support to MCIN/AEI of Spain (projects PID2020-114653RB-I00 and TED2021-131255B-C41) funded by MCIN/AEI/10.13039/501100011033 and '(MAD2D-CM)-UCM' projects funded by Comunidad de Madrid, by the Recovery, Transformation and Resilience Plan, and by NextGenerationEU from the European Union. E. O., J. C. and M. P.-E. also acknowledge the MICIN/AEI of Spain (projects PID2021-128569NB-I00, TED2021-131255B-C44 and RED2022-134939-T funded by MCIN/AEI/10.13039/501100011033 and by "ERDF A way of making Europe") and the Generalitat Valenciana (Grant No. MFA/2022/017). Project MFA/2022/017 forms part of the Advanced Materials program supported by MCIN with funding from European Union NextGenerationEU (PRTR-C17.I1) and by Generalitat Valenciana. M. P.-E. acknowledges the PRE2021-097082 grant funded by MCIN/AEI and "ESF Investing in your future". F. L., M. B. and H. U. also thank MCIN/AEI of Spain (PID2022-141687OB-I00, TED2021-131255B-C42 and RED2024-154178-T), the Junta de Comunidades de Castilla-La Mancha, and European Social Funds (SBPLY/21/180501/000142). M.B. thanks the Spanish State Research Agency for the Ramon y Cajal contract RYC2021-034815.

References

1 A. Kojima, K. Teshima, Y. Shirai and T. Miyasaka, *J. Am. Chem. Soc.*, 2009, **131**, 6050–6051.
2 L. National Renewable Energy, Best Research-Cell Efficiency Chart, **https://www.nrel.gov/pv/cell-efficiency.html**.
3 S. N. Habisreutinger, R. J. Nicholas and H. J. Snaith, *Adv. Energy Mater.*, 2017, **7**, 1601839.
4 N. Martín, *Adv. Energy Mater.*, 2017, **7**, 1601102.
5 C. Gong, H. Li, Z. Xu, Y. Li, H. Wang, Q. Zhuang, A. Wang, Z. Li, Z. Guo, C. Zhang, B. Wang, X. Li and Z. Zang, *Nat. Commun.*, 2024, **15**, 9154.
6 E. Hou, S. Cheng, Y. Qiu, X. Chen, J. Chen, C. Sun, H. Zhang, J. Yang, X. Zhao, L. Xie, Z. Chen, C. Tian and Z. Wei, *Angew. Chem., Int. Ed.*, 2025, **64**, e202416703.
7 R. Sandoval-Torrientes, J. Pascual, I. García-Benito, S. Collavini, I. Kosta, R. Tena-Zaera, N. Martín and J. L. Delgado, *ChemSusChem*, 2017, **10**, 2023–2029.
8 M. Valles-Pelarda, B. C. Hames, I. García-Benito, O. Almora, A. Molina-Ontoria, R. S. Sánchez, G. Garcia-Belmonte, N. Martín and I. Mora-Sero, *J. Phys. Chem. Lett.*, 2016, **7**, 4622–4628.
9 J. Pascual, J. L. Delgado and R. Tena-Zaera, *J. Phys. Chem. Lett.*, 2018, **9**, 2893–2902.
10 S. F. Völker, M. Vallés-Pelarda, J. Pascual, S. Collavini, F. Ruipérez, E. Zuccatti, L. E. Hueso, R. Tena-Zaera, I. Mora-Seró and J. L. Delgado, *Chem. Eur. J.*, 2018, **24**, 8524–8529.
11 A. Cabrera-Espinoza, S. Collavini, J. G. Sánchez, I. Kosta, E. Palomares and J. L. Delgado, *ACS Appl. Mater. Interfaces*, 2024, **16**, 20852–20864.
12 X.-G. Hu, Z. Lin, L. Ding and J. Chang, *SusMat*, 2023, **3**, 639–670.
13 J. Zhang, X. Hu, H. Li, K. Ji, B. Li, X. Liu, Y. Xiang, P. Hou, C. Liu, Z. Wu, Y. Shen, S. D. Stranks, S. R. P. Silva, H.-M. Cheng and W. Zhang, *Adv. Funct. Mater.*, 2021, **31**, 2104396.
14 I. Jeon, A. Shawky, S. Seo, Y. Qian, A. Anisimov, E. I. Kauppinen, Y. Matsuo and S. Maruyama, *J. Mater. Chem. A*, 2020, **8**, 11141–11147.
15 Y. Shi, G. Meng, Y. Wang, W. Li, H. Ma, R. Wang, S. Li, Z. Zhang, Z. Tian, Y. Li, L. Zhang, B. Xu, Z. Liu, T. Feng, J. Cheng, L. Liu, D. Cao, W. Tian and Y. Shi, *Adv. Energy Mater.*, 2025, 2405355.
16 T. Miletić, E. Pavoni, V. Trifiletti, A. Rizzo, A. Listorti, S. Colella, N. Armaroli and D. Bonifazi, *ACS Appl. Mater. Interfaces*, 2016, **8**, 27966–27973.
17 C. Zhang, M. Chen, F. Fu, H. Zhu, T. Feurer, W. Tian, C. Zhu, K. Zhou, S. Jin, S. M. Zakeeruddin, A. N. Tiwari, N. P. Padture, M. Grätzel and Y. Shi, *Energy Environ. Sci.*, 2022, **15**, 1536–1544.
18 K. Wojciechowski, I. Ramirez, T. Gorisse, O. Dautel, R. Dasari, N. Sakai, J. M. Hardigree, S. Song, S. Marder, M. Riede, G. Wantz and H. J. Snaith, *ACS Energy Lett.*, 2016, **1**, 648–653.
19 H. Tang, Q. Cao, Z. He, S. Wang, J. Han, T. Li, B. Gao, J. Yang, D. Deng and X. Li, *Sol. RRL*, 2020, **4**, 1900415.
20 A. M. Elseman and A. G. Al-Gamal, *ACS Appl. Nano Mater.*, 2024, **7**, 8792–8803.
21 D. Li, L. He, Z. Pang, F. Wang, L. Fan, X. Liu, M. Wei and L. Yang, *Sol. RRL*, 2022, **6**, 2200297.
22 J. Wang, R. Zhang, H. Xu, Y. Chen, H. Zhang and N.-G. Park, *ACS Energy Lett.*, 2022, **7**, 1577–1585.
23 Y. Wang, W. Li, Y. Yin, M. Wang, W. Cai, Y. Shi, J. Guo, W. Shang, C. Zhang, Q. Dong, H. Ma, J. Liu, W. Tian, S. Jin, J. Bian and Y. Shi, *Adv. Funct. Mater.*, 2022, **32**, 2204831.
24 H. Uceta, A. Cabrera-Espinoza, M. Barrejón, J. G. Sánchez, E. Gutierrez-Fernandez, I. Kosta, J. Martín, S. Collavini, E. Martínez-Ferrero, F. Langa and J. L. Delgado, *ACS Appl. Mater. Interfaces*, 2023, **15**, 45212–45228.
25 M. K. A. Mohammed, A. K. Al-Mousoi, S. Singh, A. Kumar, M. K. Hossain, S. Q. Salih, P. Sasikumar, R. Pandey, A. A. Yadav and Z. M. Yaseen, *Opt. Mater.*, 2023, **138**, 113702.
26 J. Zhang, X.-G. Hu, K. Ji, S. Zhao, D. Liu, B. Li, P.-X. Hou, C. Liu, L. Liu, S. D. Stranks, H.-M. Cheng, S. R. P. Silva and W. Zhang, *Nat. Commun.*, 2024, **15**, 2245.
27 X. Ma, T. Zhang, B. Zhao, C. Liu, X. Li, H. Liu, G. Yang, Y. Chen, L. Jiang and X. Li, *ACS Appl. Energy Mater.*, 2020, **3**, 11674–11680.
28 Y. Yang, H. Chen, C. Hu and S. Yang, *J. Mater. Chem. A*, 2019, **7**, 22005–22011.
29 A. Setaro, M. Adeli, M. Glaeske, D. Przyrembel, T. Bisswanger, G. Gordeev, F. Maschietto, A. Faghani, B. Paulus, M. Weinelt, R. Arenal, R. Haag and S. Reich, *Nat. Commun.*, 2017, **8**, 14281.
30 Y. Maeda, K. Saito, N. Akamatsu, Y. Chiba, S. Ohno, Y. Okui, M. Yamada, T. Hasegawa, M. Kako and T. Akasaka, *J. Am. Chem. Soc.*, 2012, **134**, 18101–18108.
31 M. Barrejón, R. Rauti, L. Ballerini and M. Prato, *ACS Nano*, 2019, **13**, 8879–8889.
32 A. Juzgado, A. Soldà, A. Ostric, A. Criado, G. Valenti, S. Rapino, G. Conti, G. Fracasso, F. Paolucci and M. Prato, *J. Mater. Chem. B*, 2017, **5**, 6681–6687.
33 M. Barrejón, H. B. Gobeze, M. J. Gómez-Escalonilla, J. L. G. Fierro, M. Zhang, M. Yudasaka, S. Iijima, F. D'Souza and F. Langa, *Nanoscale*, 2016, **8**, 14716–14724.

34 L. M. Arellano, M. Barrejón, H. B. Gobeze, M. J. Gómez-Escalonilla, J. L. G. Fierro, F. D'Souza and F. Langa, *Nanoscale*, 2017, **9**, 7551–7558.

35 L. M. Arellano, H. B. Gobeze, M. J. Gómez-Escalonilla, J. L. G. Fierro, F. D'Souza and F. Langa, *Nanoscale*, 2020, **12**, 9890–9898.

36 A. Faghani, I. S. Donskyi, M. Fardin Gholami, B. Ziem, A. Lippitz, W. E. S. Unger, C. Böttcher, J. P. Rabe, R. Haag and M. Adeli, *Angew. Chem., Int. Ed.*, 2017, **56**, 2675–2679.

37 M. Vizuete, M. J. Gómez-Escalonilla, J. L. G. Fierro, M. Yudasaka, S. Iijima, M. Vartanian, J. Iehl, J.-F. Nierengarten and F. Langa, *Chem. Commun.*, 2011, **47**, 12771–12773.

38 M. Vizuete, M. J. Gómez-Escalonilla, M. Barrejón, J. L. G. Fierro, M. Zhang, M. Yudasaka, S. Iijima, P. Atienzar, H. García and F. Langa, *PCCP*, 2016, **18**, 1828–1837.

39 S. Kundu, Y. Wang, W. Xia and M. Muhler, *J. Phys. Chem. C*, 2008, **112**, 16869–16878.

40 R. Voggu, C. S. Rout, A. D. Franklin, T. S. Fisher and C. N. R. Rao, *J. Phys. Chem. C*, 2008, **112**, 13053–13056.

41 M. Isabel Lucío, F. Giacalone, V. La Parola, S. Gámez-Valenzuela, F. Muñoz-Alba, M. C. Ruiz Delgado, M. A. Herrero and E. Vázquez, *Chem. Eur. J.*, 2023, **29**, e202302476.

42 M. Barrejón, S. Pla, I. Berlanga, M. J. Gómez-Escalonilla, L. Martín-Gomis, J. L. G. Fierro, M. Zhang, M. Yudasaka, S. Iijima, H. B. Gobeze, F. D'Souza, Á. Sastre-Santos and F. Langa, *J. Mater. Chem. C*, 2015, **3**, 4960–4969.

43 B. K. Price and J. M. Tour, *J. Am. Chem. Soc.*, 2006, **128**, 12899–12904.

44 W. Gao, W. Xu, J. Ye, T. Liu, J. Wang, H. Tan, Y. Lin, M. Tange, D. Sun, L. Wu, T. Okazaki, Y. Yang, Z. Zhang, J. Zhao, Z. Cui and C.-Q. Ma, *Adv. Funct. Mater.*, 2017, **27**, 1703938.

45 E. Turek, T. Shiraki, T. Shiraishi, T. Shiga, T. Fujigaya and D. Janas, *Sci. Rep.*, 2019, **9**, 535.

46 J. P. Martínez, M. Vizuete, L. M. Arellano, A. Poater, F. M. Bickelhaupt, F. Langa and M. Solà, *Nanoscale*, 2018, **10**, 15078–15089.

47 T. Yanai, D. P. Tew and N. C. Handy, *Chem. Phys. Lett.*, 2004, **393**, 51–57.

48 F. Weigend and R. Ahlrichs, *PCCP*, 2005, **7**, 3297–3305.

49 E. Caldeweyher, J.-M. Mewes, S. Ehlert and S. Grimme, *PCCP*, 2020, **22**, 8499–8512.

50 E. Caldeweyher, S. Ehlert, A. Hansen, H. Neugebauer, S. Spicher, C. Bannwarth and S. Grimme, *J. Chem. Phys.*, 2019, **150**, 154122.

51 E. Caldeweyher, C. Bannwarth and S. Grimme, *J. Chem. Phys.*, 2017, **147**, 034112.

52 T. Bu, L. Wu, X. Liu, X. Yang, P. Zhou, X. Yu, T. Qin, J. Shi, S. Wang, S. Li, Z. Ku, Y. Peng, F. Huang, Q. Meng, Y.-B. Cheng and J. Zhong, *Adv. Energy Mater.*, 2017, **7**, 1700576.

53 M. Azam, Y. Ma, B. Zhang, X. Shao, Z. Wan, H. Zeng, H. Yin, J. Luo and C. Jia, *Nat. Commun.*, 2025, **16**, 602.

54 M. Almalki, M. H. Alotaibi, A. Q. Alanazi, F. T. Eickemeyer, S. M. Alenzi, Y. A. Alzahrani, L. Piveteau, A. Y. Alymani, A. Albadri, H. Albrithen, J. V. Milić, S. M. Zakeeruddin, H. Zhang and M. Grätzel, *Adv. Funct. Mater.*, 2024, **34**, 2309789.

55 C. Tian, G. Betancourt-Solis, Z. Nan, K. Liu, K. Lin, J. Lu, L. Xie, L. Echegoyen and Z. Wei, *Sci. Bull.*, 2021, **66**, 339–346.

56 Y. Ko, Y. Kim, C. Lee, Y. Kim and Y. Jun, *ACS Appl. Mater. Interfaces*, 2018, **10**, 11633–11641.

57 Z. Dong, W. Li, H. Wang, X. Jiang, H. Liu, L. Zhu and H. Chen, *Matter*, 2022, **5**, 448–481.

58 S. Bandow, A. M. Rao, G. U. Sumanasekera, P. C. Eklund, F. Kokai, K. Takahashi, M. Yudasaka and S. Iijima, *Appl. Phys. A*, 2000, **71**, 561–564.

59 S. Shao and M. A. Loi, *Adv. Mater. Interfaces*, 2020, **7**, 1901469.

60 H. Luo, Z. Zhang, L. Yuan, J. Wang, B. Li, S. Wang, M. Abdi-Jalebi, L. Shi, W. Zhang, K. Guo, L. Ding and K. Yan, *Carbon Neutrality*, 2023, **2**, 21.

61 Z. Iqbal, F. Zu, A. Musiienko, E. Gutierrez-Partida, H. Köbler, T. W. Gries, G. V. Sannino, L. Canil, N. Koch, M. Stolterfoht, D. Neher, M. Pavone, A. B. Muñoz-García, A. Abate and Q. Wang, *ACS Energy Lett.*, 2023, **8**, 4304–4314.

62 S. You, F. T. Eickemeyer, J. Gao, J.-H. Yum, X. Zheng, D. Ren, M. Xia, R. Guo, Y. Rong, S. M. Zakeeruddin, K. Sivula, J. Tang, Z. Shen, X. Li and M. Grätzel, *Nat. Energy*, 2023, **8**, 515–525.

63 C. Plett and S. Grimme, *Angew. Chem., Int. Ed.*, 2023, **62**, e202214477.

64 M. Azam, A. A. Khan, G.-X. Liang, G.-J. Li, S. Chen, Z.-H. Zheng, U. Farooq, M. Ishaq, P. Fan, Z. Wang and Z.-G. Wang, *Sol. RRL*, 2020, **4**, 2000358.

65 J. S. Kim, J.-M. Heo, G.-S. Park, S.-J. Woo, C. Cho, H. J. Yun, D.-H. Kim, J. Park, S.-C. Lee, S.-H. Park, E. Yoon, N. C. Greenham and T.-W. Lee, *Nature*, 2022, **611**, 688–694.

66 Z. Zhu, K. Mao, K. Zhang, W. Peng, J. Zhang, H. Meng, S. Cheng, T. Li, H. Lin, Q. Chen, X. Wu and J. Xu, *Joule*, 2022, **6**, 2849–2868.

67 X. Yi, Z. Zhang, A. Chang, Y. Mao, Y. Luan, T. Lin, Y. Wei, Y. Zhang, F. Wang, S. Cao, C. Li and J. Wang, *Adv. Energy Mater.*, 2019, **9**, 1901726.

68 S. N. Habisreutinger, T. Leijtens, G. E. Eperon, S. D. Stranks, R. J. Nicholas and H. J. Snaith, *J. Phys. Chem. Lett.*, 2014, **5**, 4207–4212.

69 K. Zhu, Z. Hu and G. Chen, *Compos. Commun.*, 2022, **32**, 101166.

70 Y. Li, H. Li, C. Zhong, G. Sini and J.-L. Brédas, *npj flex. electron.*, 2017, **1**, 2.

71 D. Shi, X. Qin, Y. Li, Y. He, C. Zhong, J. Pan, H. Dong, W. Xu, T. Li, W. Hu, J.-L. Brédas and O. M. Bakr, *Sci. Adv.*, 2016, **2**, e1501491.

72 M. Pérez-Escribano, A. Fernández-Alarcón, E. Ortí, J. Aragó, J. Cerdá and J. Calbo, *Faraday Discuss.*, 2024, **250**, 202–219.

73 C. Bannwarth, S. Ehlert and S. Grimme, *J. Chem. Theory Comput.*, 2019, **15**, 1652–1671.

74 M. M. Tavakoli, J. Zhao, R. Po, G. Bianchi, A. Cominetti, C. Carbonera and J. Kong, *Adv. Funct. Mater.*, 2019, **29**, 1905887.

75 X. Chen, P. V. Kamat, C. Janáky and G. F. Samu, *ACS Energy Lett.*, 2024, **9**, 3187–3203.

76 L. Shen, P. Song, K. Jiang, L. Zheng, J. Qiu, F. Li, Y. Huang, J. Yang, C. Tian, A. K. Y. Jen, L. Xie and Z. Wei, *Nat. Commun.*, 2024, **15**, 10908.

77 E. Kasparavicius, M. Franckevičius, V. Malinauskiene, K. Genevičius, V. Getautis and T. Malinauskas, *ACS Appl. Energy Mater.*, 2021, **4**, 13696–13705.

78 S. Zeiske, O. J. Sandberg, N. Zarrabi, C. M. Wolff, M. Raoufi, F. Peña-Camargo, E. Gutierrez-Partida, P. Meredith, M. Stolterfoht and A. Armin, *J. Phys. Chem. Lett.*, 2022, **13**, 7280–7285.

79 V. J. Y. Lim, A. J. Knight, R. D. J. Oliver, H. J. Snaith, M. B. Johnston and L. M. Herz, *Adv. Funct. Mater.*, 2022, **32**, 2204825.

80 H. Baig, H. Kanda, A. M. Asiri, M. K. Nazeeruddin and T. Mallick, *Sustain. En. Fuels*, 2020, **4**, 528–537.

81 X. Liao, X. Jia, W. Li, X. Lang, J. Zhang, X. Zhao, Y. Ji, Q. Du, C.-H. Kuan, Z. Ren, W. Huang, Y. Bai, K. Zhang, C. Xiao, Q. Lin, Y.-B. Cheng and J. Tong, *Nat. Commun.*, 2025, **16**, 1164.

82 H. Uratani and K. Yamashita, *J. Phys. Chem. Lett.*, 2017, **8**, 742–746.

83 Y. Shao, Z. Xiao, C. Bi, Y. Yuan and J. Huang, *Nat. Commun.*, 2014, **5**, 5784.

84 H. J. Snaith, A. Abate, J. M. Ball, G. E. Eperon, T. Leijtens, N. K. Noel, S. D. Stranks, J. T.-W. Wang, K. Wojciechowski and W. Zhang, *J. Phys. Chem. Lett.*, 2014, **5**, 1511–1515.